



Combining shape-adaptive blades and active flow control in a multi-stage axial compressor: a numerical study

M. Seidler^{1,4} · Z. Montano^{2,4} · D. Mimic^{3,4} · N. Meinicke^{2,4} · J. Friedrichs^{1,4} · J. Riemenschneider^{2,4} · J. R. Seume^{3,4}

Received: 3 March 2023 / Revised: 22 November 2023 / Accepted: 20 December 2023
© The Author(s) 2024

Abstract

Shape adaption (SA) via piezo-ceramic actuation, and active flow control (AFC) by means of fluid injection and aspiration, are investigated within the Cluster of Excellence for Sustainable and Energy-Efficient Aviation (SE²A) with the goal of increasing the efficiency of multi-stage compressors—particularly at part-load, and of extending their operating range. Although both technologies have shown to be beneficial for the compressor off-design operation, drawbacks are still apparent at the aerodynamic design point when a single rotor or stator is equipped with SA or AFC, because of wake disturbances, which increase the incidence angle of the following row. Especially matching an improved component with its respective stage counterpart poses a major challenge in both research areas and is, therefore, addressed within this investigation. This work focuses on the first two stages of a high-pressure compressor, to compare and evaluate different combinations of shape adaption and active flow control. By considering structural requirements, such as a minimum blade thickness for the actuator application, and aerodynamic sensitivities, such as flow incidence and deviation due to off-design operation, a suitable configuration is derived and investigated in further detail.

Keywords Active flow control · Shape adaption · Multi-stage axial compressor

List of symbols

| | |
|------------------|-------------------------------|
| β | Flow deflection, ° |
| β_1 | Relative inflow angle, ° |
| c | Blade chord, m |
| δ | Flow deviation, ° |
| λ | Stagger angle, ° |
| ϵ | GCI error, 1 |
| h | Blade height, m |
| h_{tot} | Specific total enthalpy, J/kg |
| i | Flow incidence, ° |
| γ | Isentropic exponent, 1 |

| | |
|--------------------|-----------------------------------|
| κ_1 | Leading edge metal angle, ° |
| \dot{m} | Mass flow, kg/s |
| η_{is} | Isentropic efficiency, 1 |
| P | Power, W |
| p | Static pressure, N/m ² |
| φ | Profile cambering, ° |
| π | Static pressure ratio, 1 |
| π_{tot} | Total pressure ratio, 1 |
| p_{tot} | Total pressure, N/m ² |
| r | Radius, m |
| Ma' | Relative inflow Mach number, 1 |
| ρ | GCI order, 1 |
| V_m | Meridional velocity, m/s |
| y^+ | Non-dimensional wall distance, 1 |

✉ D. Mimic
mimic@tfd.uni-hannover.de

- ¹ Institute of Jet Propulsion and Turbomachinery, TU Braunschweig, Hermann-Blenk-Straße 37, 38108 Brunswick, Germany
- ² Institute of Lightweight Systems, German Aerospace Center (DLR), Lilienthalplatz 7, 38108 Brunswick, Germany
- ³ Institute of Turbomachinery and Fluid Dynamics, Leibniz University Hannover, An der Universität 1, 30823 Garbsen, Germany
- ⁴ Cluster of Excellence SE²A-Sustainable and Energy Efficient Aviation, TU Braunschweig, Universitätsplatz 2, 38106 Brunswick, Germany

Indices

| | |
|------|-----------------------|
| Acc | Acceleration scenario |
| corr | Corrected |
| def | Deformed |
| inj | Injected |
| LE | Leading edge |
| ref | Reference |
| rel | Relative |
| tgt | Target |
| tot | Total |

| | |
|----|------------------|
| t | Tip |
| ui | Unique incidence |

Acronyms

| | |
|------|---------------------------------|
| AFC | Active flow control |
| CFD | Computational fluid dynamics |
| DP | Design point |
| FEA | Finite-element analysis |
| GCI | Grid-convergence index |
| HPC | High-pressure compressor |
| IGV | Inlet guide vane |
| LPC | Low-pressure compressor |
| MFC | Macro-fibre composite |
| OGV | Outlet guide vane |
| REF | Reference |
| R | Rotor |
| RANS | Reynolds-averaged Navier–Stokes |
| SA | Shape adaption |
| SMA | Shape-memory alloys |
| S | Stator |
| UHBR | Ultra-high bypass ratio |

1 Introduction

The optimisation of the axial compressor off-design operation in modern jet engines plays a major role in the design process of such systems. With recent advancements in aircraft engine design towards a reduction of environmental pollution and CO₂ emissions, high off-design efficiency becomes increasingly important. The causes leading to off-design operation may differ: For the fan stage, the occurrence of cross wind events [1] or the ingestion of the external aircraft boundary layer [2] causes flow incidence and local total pressure deficits, which reduce the fan stage efficiency. Changing ambient conditions, mainly induced through alterations in flight altitude, also influence the fan performance. In general, flight phases that differ from the original design target lead to a shift in the fan performance, which is accompanied by an efficiency penalty or even a violation of safety margins [3]. For the high-pressure compressor (HPC) and low-pressure compressor (LPC) of the engine, transient manoeuvres are of special interest [4]. Especially for the HPC, engine acceleration temporarily shifts the compressor operating point towards the stability limit of the compressor, which significantly reduces the surge margin of the system. Combined with additional deterioration of the blading, which is known to reduce the surge margin, this might lead to unstable engine operation. Deceleration manoeuvres on the other hand, temporarily reduce the efficiency of the compressor, as the operating point is shifted closer to the choke limit of the compressor.

1.1 Flexible compressor operation

To improve off-design performance of axial compressors, different measures have been introduced. Optimised outlet guide vanes (OGV) in the fan stage of ultra-high bypass-ratio (UHBR) engines increase the incidence tolerance of the stator stages when distortion effects are transported through the transonic rotor blades [5, 6]. Next to a reduction of stage losses under inflow incidence, the operating range could be extended through an improved stator design. Within the compressor stages in the core engine, variable stator vanes are often used to improve the surge margin [7]. Through a simple pitch variation, the inflow incidence for every stator row in the multi-stage compressor is reduced, improving overall stage efficiency as well as operating range. Off-design operation of the compressor components often forces the jet engines to compensate for pressure ratio, mass flow or efficiency deficits by adapting the rotational speed. With the introduction of multi-shaft engines, the different compressor systems can be regulated more flexibly, which improves overall jet engine efficiency [3]. The build-up of end wall boundary layer in the HPC, which is exacerbated by off-design operation, can be controlled through bleed holes or active flow control measures, where the viscous and turbulent fluid is aspirated from the compressor [4].

1.2 Shape-adaptive blades

Based on stagger-variable stator vanes, the authors of [8] investigated shape-adaptive blading, where piezo-ceramic actuators were applied onto the pressure and suction sides of cascade blading during wind tunnel experiments. By subjecting the actuators to an electric field, the actuator stack-ups contract or expand, inducing a deformation of the blade body. A pitch variation of approximately 1° was thereby achievable for plastic blades. In an attempt to transfer this technology to the rotor blading of the highly transonic NASA rotor 67, the authors of [9] developed a numerical design methodology to evaluate the potential of shape morphing in a rotating compressor system. With that, an alternative to pitch-variable fan blading was created, which has been investigated in [10, 11].

1.3 Active flow control

Active flow-control (AFC) methods present a way to meet these flexibility requirements, since they allow for variable, and even transient, operation. The AFC parameters can, thus, be adapted to yield high performance benefits across a wide range of operating points and ensure a sufficient surge margin during acceleration manoeuvres. The means

of AFC investigated in this paper comprise the actuation through injection and aspiration of fluid on selected stator-vane surfaces.

1.3.1 Injection

The tangential injection of fluid into a boundary layer is arguably the most straightforward way to suppress its downstream separation. The momentum carried by the injected mass flow ‘replenishes’ the near-wall momentum deficit and allows the boundary-layer flow to overcome greater adverse pressure gradients.

The authors of [12] tested low-pressure turbine aerofoils equipped with a suction-side injection system in a cascade wind tunnel. The authors concluded that this method is especially useful for achieving high aerodynamic loading.

The authors of [13] later investigated the performance impact of compressor stators with suction-side injection and a strongly curved aft section, which makes use of the Coandă effect to increase the flow turning. These experiments, and their continuation by the authors of [14] which were carried out on the 4½-stage compressor considered in this paper, demonstrated a clear performance benefit of this approach. The beneficial influence of Coandă stators—especially under near-stall conditions—was later confirmed in [15].

1.3.2 Aspiration

Boundary-layer separation can also be suppressed by aspirating low-momentum fluid from the near-wall flow, which is then replaced by high-momentum fluid from the free stream. The use of AFC by aspiration is, thus, preferable downstream of the separation onset. Aspirating fluid from an already separated boundary layer has the additional advantage that the fluid removed carries a relatively high entropy.

The authors of [16] demonstrated decreased flow blockage and increased flow turning by aspirating fluid from the rotor blades of a transonic compressor. The authors of [17] were able to suppress corner stall by means of aspiration.

Based on a design presented in [18], the authors of [19] tested the aspiration of fluid from the first stator of a 4½-stage compressor (the same compressor, which is also considered in this paper) and achieved performance improvements even in non-actuated stages.

1.4 Goal and structure of this paper

The goal of this paper is to identify the potential of combining shape-adaptive rotor blades and AFC using injection stators with respect to an improved off-design performance. The paper individually introduces AFC and shape adaption for separate design cases, considering the respective potentials and requirements of both technologies. Based on

the initial findings, possible concepts for combining both technologies are introduced and evaluated. With the goal of reducing the individual drawbacks of each technology a suitable combination is chosen for a high-pressure compressor application, which is discussed in further detail. The paper is organised as follows:

1. The introduction provides an overview of previous work regarding shape-adaptive blades and AFC methods.
2. The aero-structural design approach for shape-adaptive blades is introduced. In this section, the well-researched NASA rotor 67 is transformed into a shape-adaptive fan blade. Potentials and drawbacks for improving off-design performance are discussed.
3. The performance impact of piezo-actuated shape adaption is presented in further detail and illustrated with the help of stationary Reynolds-averaged Navier–Stokes (RANS) single-passage simulations carried out with Ansys CFX.
4. The methodical approach for the application of injection vanes to a 4½-stage compressor model is introduced.
5. The performance impact of the injection is evaluated using stationary single-passage RANS simulations using DLR TRACE 9.4.3 [20] and potential deflection requirements are derived for the shape-adaptive blades.
6. Finally, different concepts for incorporating both technologies into one compressor are discussed using the example of a multi-stage high-pressure compressor. Different combinations of AFC and shape adaption (SA) in varying rotor and stator rows are discussed with the goal of determining a fruitful combination for further investigations.

2 Design of shape-adaptive blading

2.1 Actuation concepts and simulation

The concept of shape-morphing blading has already been investigated for stationary blading in cascade wind tunnel experiments presented in [8]. The actuators applied were macro-fibre composites (MFC), which are piezo-ceramic fibres embedded into a polymer matrix. An electric field is applied for the actuation, which causes actuators either to contract or elongate (expand), depending on the polarity. The elongation achievable by MFC actuators is about three times larger than their contraction [21]. Through the fibre orientation of the composite actuators the direction of the deformation can be adjusted. A simulation methodology for the actuation concept was developed in [9] to facilitate numerical investigations. To model the actuation a thermal analogy is applied instead of a regulation voltage, which induces equivalent deformations through temperature

boundary conditions for the actuators. By embedding the actuators into the compressor blading, the deformations are transferred into the blading, leading to a variation of the blade angles and, therefore, to a modification of the stage aerodynamics. In the simulation approach, the reference blading is considered to be made of titanium alloys, since this is currently the most common material for compressor blades. However, other materials are possible, such as carbon-fibre reinforced composites.

As the application of MFC actuators to the well-researched NASA rotor 67 has shown that the achievable deformations are limited to a maximum of 1.3° for the blade profile cambering and the leading-edge metal angle, an alternative actuator concept is considered within this research. Shape-memory alloys (SMAs) are nickel–titanium-based alloys which can exhibit superelastic and shape-memory effects under different thermal and stress conditions. An exposure of SMAs to different thermal conditions can lead to a change in the SMAs shape. Similar to MFC actuators, SMA fibre or sheet-based actuators could be embedded into compressor blading to induce a shape-morphing effect exploiting their temperature sensitivity. The technical application of these active materials and the induction of pre-defined deformations however require a training process for the material to memorise its shape under different environmental conditions. Due to the high energy density of SMA materials, the morphing potential is significantly higher, as are the expectable deformations. However, contrary to MFC actuators, SMA aerofoil actuators for compressor blading still need to be developed to be able to take advantage of the active material properties and to be able to embed them in compressor blades. Hence, within the study presented the geometric boundary conditions for the integration of SMAs, meaning their sizes and positions in the blades, are assumed to be equal to those of the MFC actuators. The temperature boundary conditions for the thermal analogy are chosen differently for each material, so as to adequately match the achievable deformations of the MFCs through an electric field, as well as those of the SMAs via their operational temperatures.

2.2 Coupled design methodology

Within the research of shape-morphing blading, the well-documented NASA rotor 67 described in [22] was transformed into a shape-adaptive system. Figure 1 presents the meridional view the NASA stage 67, with the orange colouring indicating the shape-adaptive NASA rotor 67.

By coupling aerodynamic and structural design methodologies, the morphing potential of a shape-adaptive NASA rotor 67 was assessed. A detailed description of the applied numerical computational fluid dynamics (CFD) and finite-element analysis (FEA) methodologies

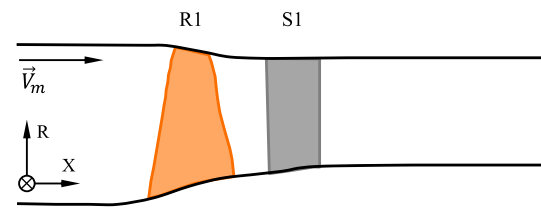


Fig. 1 Meridional view of NASA stage 67

is given in [9]. Aerodynamic design stream sections were created and are kept constant throughout the design process. Thereby, a three-stage coupling of increasing fidelity was obtained. The main iterative procedure for the selection of a suitable actuation concept is conducted in the first step, where the span-wise morphing of the blade angles is evaluated through a comparison with aerodynamic morphing requirements. The morphing requirements are derived from a pre-defined morphing scenario and specified through a streamline curvature calculation as described in [23]. The basic assumption of this procedure is to select a new design point for which a new design point (DP) geometry is derived. By comparing the inflow angle as well as the flow turning requirement of the new design point to the reference design flow condition, aerodynamic morphing requirements are specified. The actuation concept is then optimised to match the aerodynamic requirements specified. Previous research has shown that the achievable deformations here are largest towards the blade tip due to the hub-side blade mounting. This allows to specify the stagger angle and blade camber angle morphing at the blade tip as a representative optimisation parameter. While the actuation concept can be modified through a variation of the actuation direction, actuator sizes and actuation mechanism (expansion, contraction, or inactive), the aerodynamic off-design conditions are aligned with the structural requirements by adjusting the inflow velocity distribution as well as the hub loading of the rotor. In the last and numerically most expensive step, the deformed rotor geometry is fully re-engineered and numerically evaluated through stationary 3D RANS stage simulations. Within the re-engineering process it is assumed that the blade profile morphing is captured fully by the camber morphing, which allows the thickness distribution to remain unchanged throughout the aerostructural design process [24]. Special emphasis within the re-engineering process lies on the evaluation of the leading-edge metal angle and the profile turning, as the morphing of both parameters directly influences the mass flow as well as the achievable pressure ratio of the stage. Additionally, the suction-side curvature and the throat-area variation are considered for the evaluation of the achievable morphed shapes. The re-engineering is finalised by

Table 1 Grid-convergence indices

| | η_{is} | \dot{m} | π_{tot} |
|-----------------|------------------------|------------------------|------------------------|
| ϵ_{21} | -3.43×10^{-4} | -3.59×10^{-4} | -3.01×10^{-5} |
| ϵ_{32} | -1.14×10^{-4} | -2.09×10^{-4} | -7.86×10^{-5} |
| ρ | 1.33 | 2.71 | -2.37 |
| GCI_{21} | 1.01×10^{-4} | 1.41×10^{-3} | -1.59×10^{-4} |
| GCI_{32} | 2.73×10^{-4} | 1.71×10^{-3} | -6.09×10^{-5} |

applying the aerodynamic thickness distribution onto the morphed and re-engineered profile camber to prepare the morphed blading for the CFD evaluation.

2.3 CFD evaluation

After the re-engineering of the blade geometry, stage simulations are conducted in Ansys CFX. One rotor and stator passage are simulated with a structured mesh and a non-dimensional wall distance y^+ of approximately unity at all domain walls. The independence of the flow solution from the mesh was evaluated according to the grid-convergence index (GCI) [25]. The grid convergence was evaluated for the isentropic efficiency η_{is} (Eq. 2), the rotor pressure ratio π_{tot} (Eq. 1) and the mass-flow rate \dot{m} . According to Table 1, a mesh with approximately 6.5×10^6 cells is sufficiently fine to capture the shape-morphing effects, while exhibiting an asymptotic grid-convergence behaviour. To evaluate the influence of shape morphing two speed lines of the performance map are simulated by adjusting the rotational speed and gradually increasing the back pressure of the stage until increasing instabilities exceed the capabilities of the stationary simulation approach, indicating the numerical onset of stall. For the turbulence model, a $k-\omega$ approach was selected.

3 Shape-adaption results

For the selection of an operational scenario the performance map of the chosen test case, the actuated NASA rotor 67 geometry was simulated for four rotational velocities at 100%, 95%, 90%, and 85% of the design speed of 16,043 rpm. The speed line characteristics of the chosen test case and the effect of the introduced active flow control mechanisms are evaluated by variations of the ratio of the total pressures p_{tot} at the domain inlet (in) and outlet (out),

$$\pi_{tot} = \frac{P_{tot,out}}{P_{tot,in}}, \quad (1)$$

as well as the isentropic efficiency, defined as the ratio of reversible (rev) and irreversible (irr) power P ,

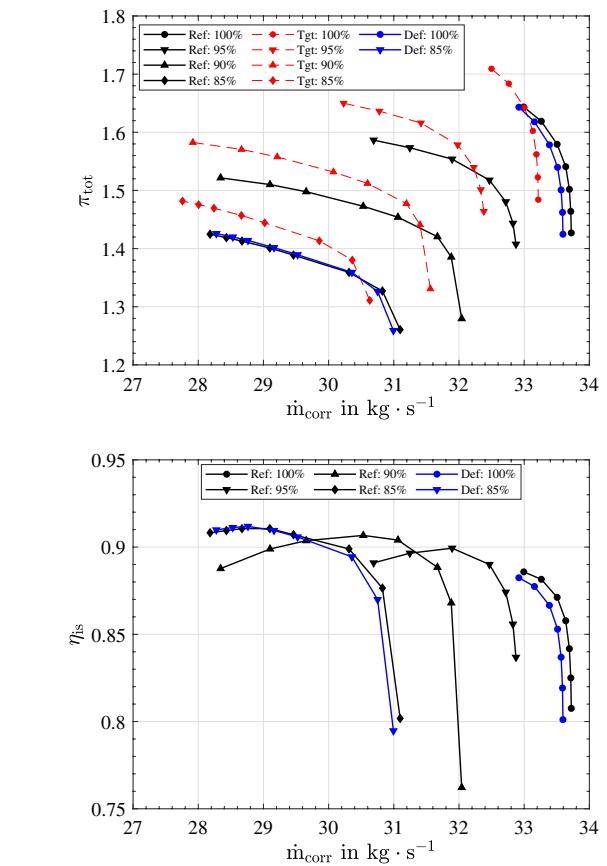


Fig. 2 Performance of the reference NASA stage 67 (black), the idealised target performance (red) and the achievable shift through shape adaption (blue)

$$\eta_{is} = \frac{P_{rev}}{P_{irr}}. \quad (2)$$

Both parameters are displayed in Fig. 2 against the corrected mass-flow rate.

As the AFC is applied to a HPC test bench, the acceleration manoeuvre is selected as a suitable scenario for this research. Based on the simulated design point of the NASA stage 67, the surge margin is determined as 23% according to the definition in [4]. With the goal of increasing the surge margin during the transient acceleration manoeuvre, the surge margin of the simulated design point is assumed to be reduced to 9% which defines a new design point (DP) for the target shape design at $\pi_{tot} = 1.65$ and $\dot{m}_{corr} = 32.71$ kg/s for the 100% speed line. By adjusting the blade shape according to the selected off-design point, a shift of the entire performance map to higher pressure ratios and reduced mass-flow rates is expected, as schematically displayed in Fig. 2.

Calculating the meridional flow distribution for the selected acceleration off-design point (Acc) and evaluating the span-wise inflow angle variation,

$$\Delta\beta_1(r) = \beta_{1,DP}(r) - \beta_{1,Acc}(r), \quad (3)$$

as well as the variation in the span-wise flow deflection,

$$\Delta\beta(r) = \beta_{DP}(r) - \beta_{Acc}(r), \quad (4)$$

relative to the reference design point shows the highest morphing requirements for the blade turning in the hub and tip regions of the rotor (Fig. 3). The structurally feasible deformations of the leading-edge metal angle,

$$\Delta\kappa_1(r) = \kappa_{1,ref}(r) - \kappa_{1,def}(r), \quad (5)$$

and the achievable morphing of the span-wise blade camber angle

$$\Delta\varphi(r) = \varphi_{ref}(r) - \varphi_{def}(r), \quad (6)$$

are then calculated to evaluate the suitability of the actuation concept. A comparison of the required inflow and flow turning variation with the achievable blade angle morphing is given in Fig. 3, depending on the fraction of leading edge radius r and the blade height h . Here AERO refers to the aerodynamic morphing requirement, while FEM labels the structurally achievable shape adaption. Similar to the required increase in the flow deflection, the depicted blade turning morphing is largest towards the blade tip, but too small to achieve the expected variation in the flow turning (Fig. 3, left). With a maximum of 0.68° , the deviation between aerodynamic requirements and structurally feasible deformations rises towards the blade hub. Because of the rigid mounting of the rotor, no deformations are induced in this area.

Due to the reduction of the design point mass flow, a higher span-wise blade metal angle is required for the new design point. The aerodynamic metal angle morphing

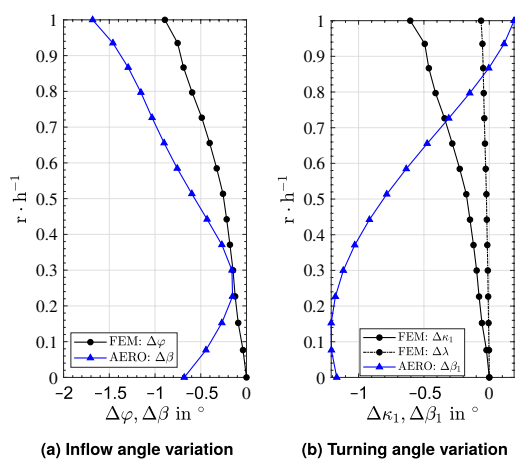


Fig. 3 Comparison of aerodynamically required flow adaption with structurally achievable deformations

requirement is mainly located below 60% of the rotor height h , while a reduction of the morphing requirement is visible towards the blade tip. With that, the achievable metal angle variation differs from the aerodynamic requirements. For the MFC actuation a deformation maximum of 0.6° is visible at the blade tip, which becomes gradually smaller towards the hub (Fig. 3, left). The leading-edge metal-angle variation is mainly induced through the variation of the blade cambering, while the span-wise stagger angle adaption remains below 0.1° .

The simulative evaluation of the morphed shapes was conducted for 100% and 85% of the design rotational speed (Fig. 2). For the 100% speed line the behaviour of the morphed rotor shapes is highly dependent on the elevated relative inflow Mach number ($Ma' = 1.38$) and therefore on the unique incidence condition. According to [26], the variation of the leading-edge metal angle induces a variation of the unique incidence angle. In this case, the unique incidence angle β_{ui} is raised, which reduces the mass flow and shifts the speed line to lower mass flows, as depicted in Fig. 2. Although, the blade turning is higher, lower pressure ratios are achieved over the entire operating range. The higher suction-side curvature of the morphed blading induces a higher pre-shock flow acceleration and therefore increases the shock magnitude, which elevates the shock losses and leads to the lower isentropic efficiencies depicted in Fig. 2 (bottom). The lower relative inflow Mach numbers of the 85% speed line limit the dependency of the rotor performance on the unique incidence condition. Towards the choke limit of the speed line, this dependency is comparable to the 100% speed line and leads to a reduction in the mass-flow rate and expectably lower efficiencies. With increasing back pressures, the passage shock moves towards the leading edge and detaches. With this, the variation of the stage efficiency as well as the flow turning depend increasingly on the morphing of the blade turning beyond the compression shock. The speed line of the morphed rotor geometry is slightly lifted above the reference speed line, while the higher flow turning capability of the rotor sections above 70% of the rotor height improve the overall stage efficiency towards the stability line of the compressor stage. Although the effect of the piezo-ceramic actuation is visible for both speed lines in Fig. 2, achieving the idealised target performance is not feasible with MFC actuators. For the 100% speed line, the increased suction-side curvature and therefore the elevated shock losses diminish the pressure rise capability of the morphed rotor. With reduced rotational speeds, the significance of the Mach number effect becomes smaller. It follows that the morphing of the blade turning is too low to achieve the overall expected shift in the speed lines and has to be elevated in future designs.

3.1 Shape-adaptive rotor vs. stator

The shape-adaptation technology can be applied to the rotor and stator blading of the stage. Even though the NASA rotor 67 was selected for the initial study, the stator blading was taken into consideration. Comparing the role of the stator and the rotor in achieving a pressure rise throughout the stage shows that deforming or adapting the rotor introduces more degrees of freedom into the design process. By deforming the rotor blading, the work input as well as the mass flow through the stage can be adjusted, while a stator is always limited by the work input of the rotor blading. With an adaptive morphing of the stator blading, only the mass flow and the stage efficiency are free design parameters. Both design parameters are already covered by variable stator vanes, which have proven their benefit in various engine architectures [4]. By morphing the rotor shape, the work input can be altered, mainly by influencing the span-wise blade profile cambering. This offers a shift of the whole performance map, while the stator blading only allows for an optimisation within the boundaries of the rotor work input. However, the potential weight reduction of stator vanes compared to a variable stator-vane system needs to be researched further. Since structurally integrated actuation requires fewer components than variable stator-vane systems, shape-adaptive vanes could reduce the system weight and complexity, potentially leading to an improved efficiency via structural design measures.

3.2 Impact of blade geometry on morphing

Preliminary shape-variation studies of the original NASA rotor 67 have shown that the expectable global deformations through a MFC actuation improves with the blade size. Depending on the orientation of the MFC actuators, either the blade chord c , the blade height h or both parameters can be adjusted to achieve a higher morphing potential. However, whether the global increase in the deformations achievable directly translates into an elevated aerodynamic angle morphing strongly depends on the blade reference shape and the actuator configuration. For smaller blading in terms of chord length and higher hub-to-tip ratio, it is likely that the deformations feasible are smaller than the ones displayed in Fig. 3. The chord length as well as the hub-to-tip ratio are therefore identified as central boundary conditions for the applicability of a piezoceramic actuation concept. Additionally, the blade maximum thickness and its distribution limit number and size of the actuators, as the actuators are integrated within the blade body and therefore locally require a minimum blade thickness of 2 mm, in case one actuator stack-up is used per actuating side. With a lower thickness, the number of actuators has to be reduced, which again limits the morphing potential.

3.3 Influence of relative inflow Mach number

For transonic inflow conditions, the intensity of blade-shock interaction is significantly altered through the suction-side curvature of the respective profile sections. When the flow upstream of the shape-adaptive rotor becomes transonic, the alteration of the suction side curvature needs to be considered as an additional design parameter. For high Ma' values, the impact of small variations in suction-side curvature, throat area and leading-edge metal angle are magnified. Decreased rotational speeds and design point mass flows weaken the Mach number effect, giving more emphasis to the camber turning variation of the transonic blade sections. This also changes the visible effect of shape adaption, especially for reduced mass flows towards the stability line of the compressor. As Fig. 2 showed, the overall morphing effect on the aerodynamic performance is reduced with the relative inflow Mach number. Its increase is therefore beneficial for the aerodynamic effect of shape adaption, especially when the expectable morphing of the stagger and turning angle remains below 1.0° .

4 Application of injection vanes

The application of injection vanes aims at the suppression of flow separation downstream of the injection slots. Especially in operational scenarios where the compressor operates under part-load conditions, flow separation in the stator vanes may diminish the pressure rise capability of the rotor and with it the overall compressor efficiency. Under consideration of the previously selected transient acceleration manoeuvre, the integration of flow injection is expected to improve the stage efficiency towards reduced mass-flows rates.

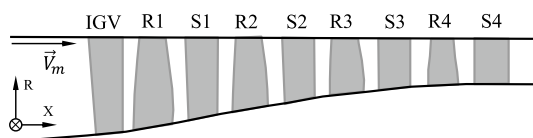
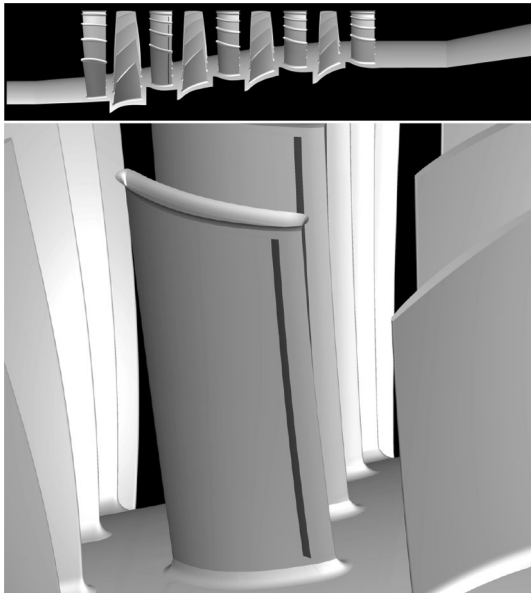
4.1 Compressor test rig

The numerical studies presented in this paper are based on the $4\frac{1}{2}$ -stage axial high-speed compressor test rig of the Institute of Turbomachinery and Fluid Dynamics at the Leibniz University Hannover. A meridional view of the compressor is displayed schematically in Fig. 4.

Experimental data from this compressor were used to validate the reference simulation model. The compressor features a fixed inlet guide vane (IGV) row followed by four stages with controlled-diffusion aerofoils. An annular diffuser with divergent hub and casing walls is located downstream of the bladed section. Table 2 provides an overview of the most relevant compressor performance parameters.

Table 2 Performance data of the 4½-stage axial compressor at the aerodynamic design point

| | |
|--|-----------------|
| Rotor speed | 18,000 rpm |
| Mass-flow rate | 7.93 kg/s |
| Total-pressure ratio | 2.72 |
| Isentropic efficiency | 89.13% |
| Power | 952 kW |
| Inlet total pressure | 60 kPa |
| Flow coefficient (first stage) | 0.72 |
| Loading coefficient (first stage) | 0.44 |
| Inflow Mach number at tip of rotor 1 | 1.005 |
| Circumferential velocity at the blade tips | 320 m/s |
| Reynolds number (stator 1) | 4×10^5 |

**Fig. 4** Meridional view of the 4½-stage axial compressor with inlet guide vane (IGV)**Fig. 5** Numerical domain of the 4½-stage axial compressor (top), injection slot in stator 1 (bottom); flow direction from left to right

4.2 Injection methodology

The numerical domain is shown in Fig. 5 (top). Two different test-case configurations were investigated numerically. Configuration REF represents the reference compressor without

any AFC ports. The AFC configuration features a jet injection on the suction side of stator 1, as shown in Fig. 5 (bottom). The AFC stator design used here was put forward in [13] and later modified and investigated in [14]. The injection mass-flow rate was set to 1.1% of the inlet mass flow for all cases.

4.3 Numerical model

The numerical simulations were carried out using the turbomachinery flow solver TRACE 9.4.3 [20], which is developed by the German Aerospace Center (DLR). All simulations are steady and feature mixing planes between rotor and stator domains. The $k-\omega$ shear-stress transport (SST) turbulence model [27] and the $\gamma-Re_\theta$ transition model [28] were used together with a stagnation-point anomaly fix [29]. The finite-volume method uses a second-order spatial discretisation. The state variables are computed using a Fromm scheme and a van Albada-square limiter. An incomplete lower–upper (ILU) factorisation is used for solving the governing equations.

The simulation domains were discretised with a structured meshing approach. The meshes comprise 9.8×10^6 cells for the reference and 12.1×10^6 cells for the AFC configuration. With some local exceptions (e.g., stagnation points), non-dimensional wall distances y^+ are kept below unity. A grid-convergence study presented in [30] concluded that no significant sensitivity of the numerical reference case was present with respect to the mesh resolution.

The inlet total pressure and temperature at the midspan were set to 60 kPa and 288.15 K, respectively. Separate inlet-duct simulations were carried out to generate realistic radial inflow distributions. A constant turbulent length-scale was assumed at the inlet. The rotor speed was set to 95% of the design speed. The outlet static pressure was iteratively increased along the speed line until convergence could no longer be achieved or reversed flow occurred.

4.4 Validation

To ensure that the numerical approach is suitable for predicting the compressor performance accurately, Fig. 6 compares the measured total-pressure ratio and isentropic efficiency of the 4½-stage compressor test rig and the corresponding numerical prediction. The numerical model predicts the compressor performance largely within the measurement uncertainty with some minor discrepancies towards the operating limits of the compressor.

5 Impact of injection vanes

The following section discusses the influence of injection on the integral compressor performance, as well as the individual compressor stages.

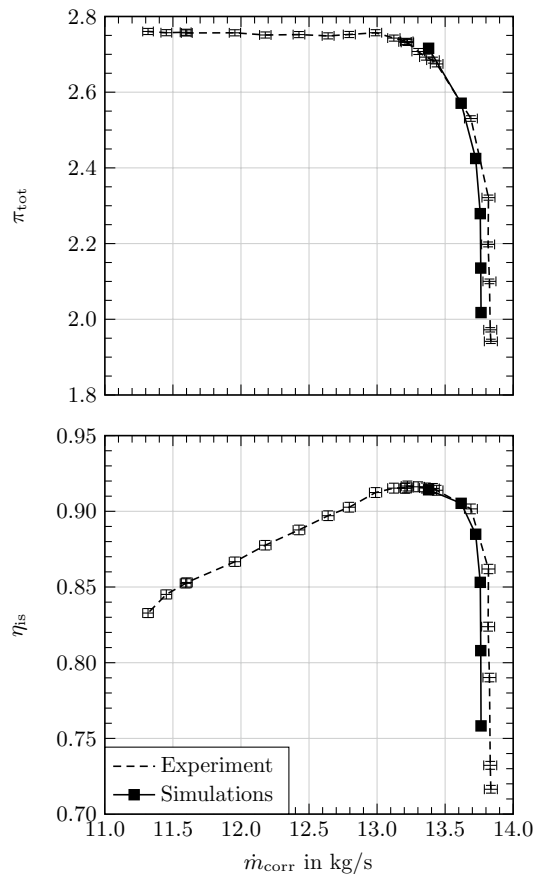


Fig. 6 Compressor speed line at 95% of the design speed: experimental data show 95% confidence intervals [30]

5.1 Compressor performance

The overall effect of AFC on the compressor performance is determined according to Eqs. 1 and 2. Additionally, the variation in static-pressure ratio,

$$\pi = \frac{p_{\text{out}}}{p_{\text{in}}}, \quad (7)$$

is accounted for. The irreversible compressor power P_{irr} for an AFC system is defined to include the enthalpy flux across the injection boundary:

$$P_{\text{irr}} = \dot{m}_{\text{out}} h_{\text{tot,out}} - \dot{m}_{\text{in}} h_{\text{tot,in}} - \dot{m}_{\text{inj}} h_{\text{tot,inj}}. \quad (8)$$

Likewise, the reversible compressor power P_{rev} is formulated so as to account for the isentropic compression processes from the injection slot to the outlet, as well as from compressor inlet to outlet:

$$P_{\text{rev}} = (\dot{m}_{\text{out}} - \dot{m}_{\text{inj}}) h_{\text{tot,in}} \left(\frac{p_{\text{tot,out}}}{p_{\text{tot,in}}} \right)^{\frac{\gamma-1}{\gamma}} - \dot{m}_{\text{in}} h_{\text{tot,in}} + \dot{m}_{\text{inj}} h_{\text{tot,inj}} \left(\frac{p_{\text{tot,out}}}{p_{\text{tot,inj}}} \right)^{\frac{\gamma-1}{\gamma}} - \dot{m}_{\text{inj}} h_{\text{tot,inj}}. \quad (9)$$

As it can be seen from the definitions above, a vanishing AFC mass-flow rate leads to the commonly used formulation of the isentropic efficiency.

Figure 7 shows the overall influence of AFC on the integral performance parameters of the compressor. It appears that the AFC speed lines exhibit a shift towards both higher corrected mass-flow rates and greater total-pressure and static-pressure ratios, respectively. Regarding the isentropic efficiency, the front-stage injection achieves efficiencies similar to the reference case under near-stall conditions.

5.2 Stage performance

Active flow control by means of fluid injection into the first stator domain yields higher overall static and total-pressure ratios of the compressor. This raises the question, which stages are the main contributors to the observed behaviour.

Figure 8 shows the performance parameters of the first two individual compressor stages. The third and fourth stage remain largely unaffected by the AFC. Here, the control domain of the first stage excludes the IGV, whereas the control volume of the last stage includes the downstream diffuser. All mass-flow rates are corrected using the total quantities at the inlet of the respective stage control domain.

5.2.1 First stage

Merely a small increase in the static-pressure ratio of the first stage can be observed as a direct result of the injection in stator 1 and the resulting increment in flow turning. The compression work in stage 1 remains unaffected because the injection is located downstream of rotor 1. The stage efficiency, however, decreases due to the additional work required for injecting the fluid.

5.2.2 Second stage

The most drastic changes occur in the second stage, i.e., downstream of the injection. Here, the use of AFC leads to a strong rise in the static and total-pressure ratios across the entire stage operating map and a shift towards higher corrected mass-flow rates. The isentropic stage efficiency behaves in a very similar way. However, the efficiency benefit of AFC, which reaches up to approx. 0.8 percentage

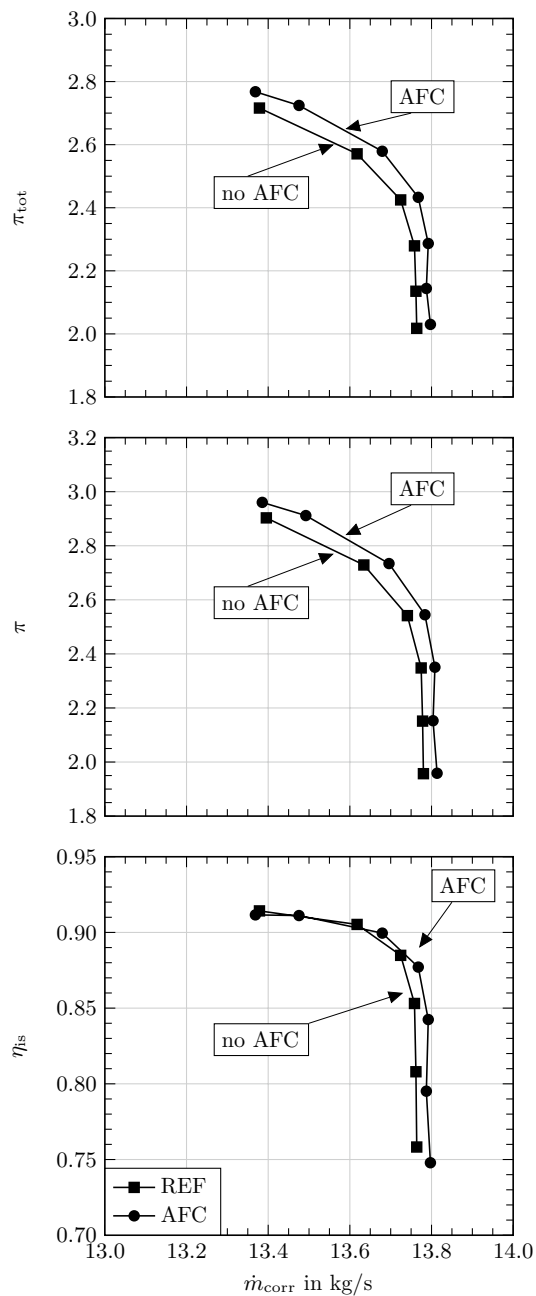


Fig. 7 Influence of AFC on the compressor performance at 95% of the design speed

points near the choke limit of the reference case, diminishes slightly towards the numerical surge line.

5.3 Shape-adaption requirements for active flow control

Figure 9 (left and centre) compares the incidence ι and deviation angles δ as a function of the relative rotor height h_{rel} of rotor 2 for the last stable operating points of REF and AFC

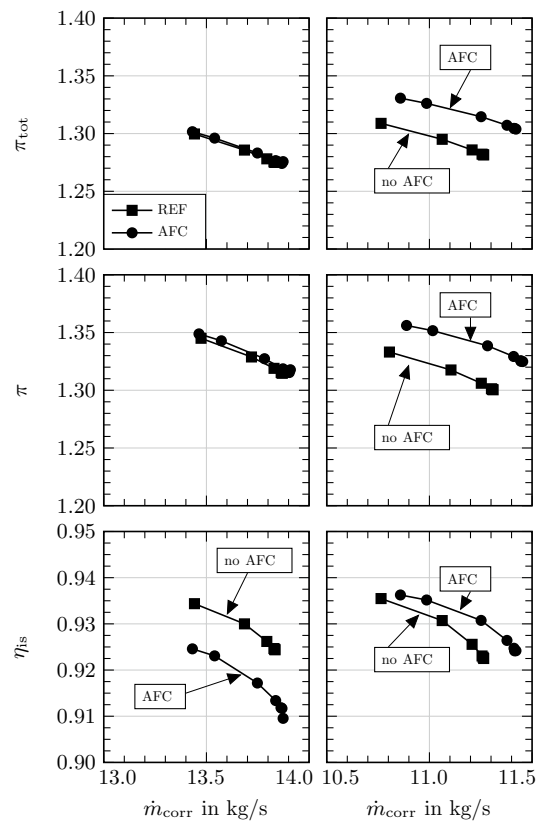


Fig. 8 Predicted speed lines at 95% of the design speed for stages 1 (left) and 2 (right)

before numerical surge is reached. The higher turning of the upstream AFC stator causes an overall higher incidence towards rotor 2. At the same time, the deviation angle downstream of rotor 2 is significantly less sensitive towards the stator 1 outflow. As a result, the rotor blades experience an elevated aerodynamic loading for the AFC configurations, which ultimately leads to an higher work input and pressure rise across the second stage, as well as higher losses towards the surge limit as the incidence-related losses likely increase.

The higher incidence, however, may be compensated by shape adaption of the downstream stator. It is expected that this would lead to a decrease in total-pressure losses and an increase in specific stage work. To achieve this, a downstream shape-adaptive rotor would need to change the leading-edge metal angle by approx. 1.5° across most of the blade span.

6 Coupling active flow control and shape adaption

6.1 Coupling concepts

Off-design operation of axial multi-stage compressors is induced mainly through variations in their rotational speed.

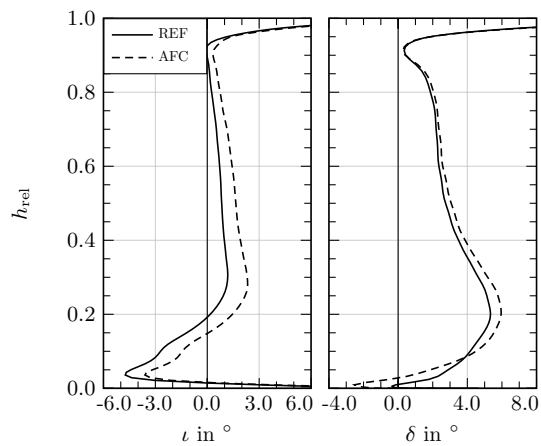


Fig. 9 Radial distributions of the incidence (left) and deviation angle (right) of rotor 2; last stable operating point before numerical surge

During off-design operation, the first and last stages of the compressor are affected especially. Depending on whether the rotational speed is increased or decreased compared to the design speed line, the first and last stages are reversely choked or stalled, while a transitional pivot stage emerges somewhere in the middle of the multi-stage compressor, which remains in its design point [3].

Since the acceleration manoeuvre considered starts at reduced rotational speeds, the total pressure ratio is significantly lower in the beginning of the manoeuvre. The tapering of the channel end-walls is, therefore, too strong, which raises the axial velocity throughout the compressor, choking the rear stages due to a negative flow incidence. Meanwhile the loading of the first stages increases, pushing their operating point towards the stability line of the compressor [4].

This indicates the highest potential for active flow control mechanisms for the front and rear stages of a multi-stage compressor, as shown in Sect. 4. Considering operation with design speed, [26] additionally stated that deviations of the first stage operating point are amplified throughout the compressor. The first stage is therefore ideally suited for a combined application of active flow control and shape-adaptive blading, as reducing flow incidence, deviation and losses in the first two stages decreases the extent to which the following stages become mismatched [26]. Choosing the first 1½ stages coincides well with the structural requirement for sufficiently high chord lengths, hub-to-tip ratios as well as respective blade thicknesses. For the combination of AFC with shape-adaptive blading within the front stage, four different combinations are selected (Fig. 10).

In general, shape adaption is applicable to the rotors, the stators, or the IGV of the first two HPC stages. Within the geometrical constraints introduced in Sect. 3.2, the IGV as well as the first rotor R1 are best suited, as they possess

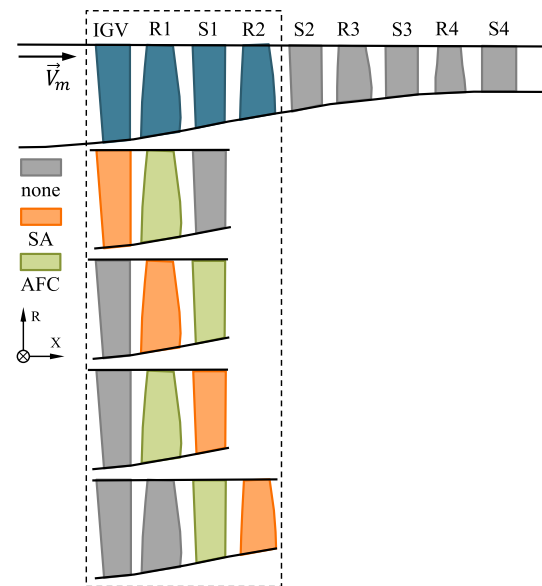


Fig. 10 Different combinations of shape-adaptive blading and active flow control within the first two stages of the 4½-stage axial compressor

the greatest suction and pressure side areas within the compressor and a blade thick enough. Among the three components, a shape-adaptive rotor additionally allows to modify the working input of the stage. Considering the Mach number requirement of shape-adaptive rotor blading, the rotor R1 outweighs the IGV. However, due to the high rotational speeds of the high-pressure compressor, the rotor has to be clamped over the whole chord length, which significantly reduces the feasible deformations (see Fig. 3). The IGV, conversely can be designed with a penny foot fixture, which has also been used by the authors of [8] and allows shifting the clamping in chord-wise direction. This gives an additional degree of freedom to the structural morphing simulation. Considering current compressor set-ups, the benefits of shape-adaptive IGVs are limited compared to pitch variable IGVs, only the downstream rotor and stator are left for the application of shape adaption (SA). However, integrating flow injection in the rotor rows is challenging when the test-rig constraints are taken into consideration. This further reduces the possible SA and AFC combinations to set-ups where the injection is implemented in the first stage stator:

1. According to the results presented in Sect. 5.3, applying the shape-adaptive rotor blades downstream of the injection stator appears to be a promising approach, as it still provides the performance benefits of the injection while mitigating the additional losses generated in the subsequent rotor. Compared to a mere restaggering of the

rotor blades in question, the shape-adaption approach allows the operating-point-dependent compensation of variations in incidence—a feature which is indispensable with regard to transient application. The choice of the second rotor, however, would reduce deformability as the chord length, profile thickness and hub-to-tip ratio are less suited to shape morphing.

- When special emphasis is given to the structural as well as aerodynamic morphing requirements, the first stage rotor would be the ideal choice, since the combination of the amplifying inflow Mach number effects with the increased deformability of the first rotor is beneficial for increasing shape-morphing potential. Flow injection in the downstream stator row (S1) could reduce its inflow incidence and, therefore, suppress possible flow separation in the stator that is likely to be provoked through the shape variation of the upstream rotor R1.

6.2 Application of shape adaption in an AFC system

Due to their specific aspect ratio and hub-to-tip ratio, the first and second stage rotors are considered as shape-adaptive components. With both rotors having a similar thickness-to-chord ratio and blade design, an analogous morphing behaviour is assumed for both rotors. For the following investigation, the first stage rotor is assumed to be shape-adaptive, while flow injection is applied to the first stage stator. Even though the impact of AFC on the flow incidence and deviation is already described in Sect. 4, the morphing potential of the first stage rotor (R1), and subsequently of R2, remains to be assessed. Considering the first stage rotor deformations to be also representative for the second stage rotor R2, it is possible to evaluate both combined configurations within this section.

By creating and revolving equidistant streamlines around the machine axis, the three-dimensional (3D) CAD model of the first stage rotor is sliced, creating point clouds of its span-wise profile sections. The methodology described in [24] is applied to identify the section-wise leading and trailing edges, to separate the pressure and suction sides, and

to re-engineer the profile camber. This allows to assess the stagger λ and turning angle φ of the morphed geometry and hence their span-wise morphing. The achievable shape morphing is depicted in Fig. 11 for an MFC and SMA actuation respectively. Details regarding the material and structural modelling for both concepts can be found in [9, 31, 32]. In Fig. 12 the aerodynamic morphing potential is quantified through the feasible variation of the leading-edge metal angle and the blade profile turning—both as functions of the normalised leading-edge radius.

The results for the piezo-ceramic actuation confirm the shape-adaption requirements, derived in Sect. 3.2. By decreasing the blade height, as well as through a reduced span-wise chord, the possible deformations are diminished. The comparison of the dimensions of the HPC rotor reference geometry with those of the NASA rotor 67 in Table 3 shows a reduction in the chord length c and blade height h_{LE} at the leading edge (LE) by 54% and 42%, respectively (Table 3).

This tendency is amplified by the reduced blade thickness towards the blade tip, which only allows for the suction-side actuator to be extended up to the tip of the rotor. The pressure side actuator only reaches up to 80% of the blade height with the piezo-ceramic actuation concept, as the blade profile thickness does not support two actuators in total. The lower design pressure ratio of the HPC rotor provokes

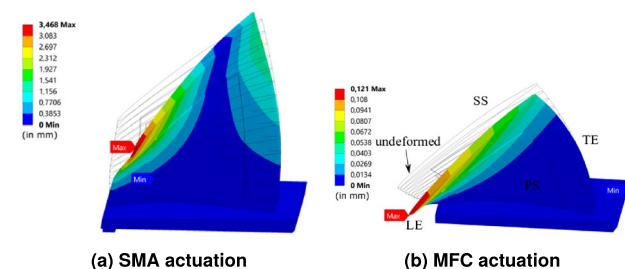


Fig. 11 Shape morphing with SMA and MFC actuation (deformations amplified for visualisation)

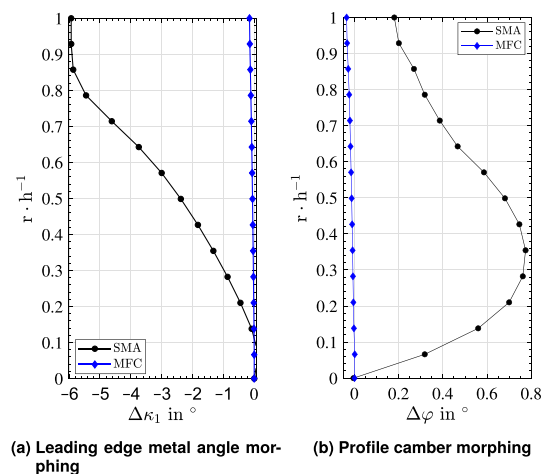


Fig. 12 Aerodynamic quantification of SMA and MFC deformations

Table 3 Overview of design parameter variation

| | HPC R1 | NASA rotor 67 |
|-----------------|--------|---------------|
| π_{tot} | 1.31 | 1.63 |
| c | 43 mm | 95 mm |
| h_{LE} | 93 mm | 160 mm |
| $Ma'(r_{1,LE})$ | 1.005 | 1.38 |

a weaker blade cambering towards its root, which favours the occurrence of 3D deformations instead of an aerodynamic blade angle morphing. With a significantly lower relative inflow Mach number at the blade tip, the aerodynamic morphing effect is expected to benefit less from the occurrence of a compression shock in the tip region of the rotor (see Fig. 2 and Sect. 3.3). Therefore, a second actuation concept is introduced, where SMA actuators are applied to the pressure and suction sides of the rotor. Similar to the MFC actuation, the target of the SMA actuation is designed to increase the span-wise stagger angle of the blade. The application of the SMA material significantly elevates the achievable deformations, despite their small dimensions (Fig. 12). In comparison with the MFC actuation, which only achieves a leading-edge metal-angle morphing of 0.15° , the SMAs can improve the maximum deformation to 5.9° . For both cases, the metal angle morphing occurs mainly through an adaption of the blade stagger angle. While the morphing of the span-wise blade cambering through MFC actuation is negligible, a reduced profile turning of 0.77° degrees can be obtained with the SMA configuration. Additionally, this morphing distribution does not follow the previous observations, where the maximum deformation was always located near the blade tip. A deformation maximum builds up at approximately 35% blade height, where the actuators end. This indicates a further difference compared to the MFC actuation for the selected HPC rotor.

6.3 Discussion

The results show that the flow deflection of a shape-adaptive rotor R1, induced by an SMA actuation, is, however, too high to be compensated by a potential active flow control mechanism in stator S1. For combining a shape-adaptive rotor R1 with the AFC stator S1, the achievable deformations need to be tailored to match the incidence as well as deviation correction capabilities of the introduced flow injection, which lie in the range of 0.2° – 1.3° .

The analysis of the AFC effects shows that for a given compressor, AFC using injection stators enhances off-design performance. The additional turning caused by the injection stator, however, causes a higher incidence towards the downstream rotor. Here, shape-adaptive rotor blades could present a way to mitigate the incidence increments and, therefore, to reduce total-pressure losses and to increase the specific stage work. Especially in the tip region of the second rotor (R2), which is most sensitive towards the flow incidence, reducing the AFC-induced incidence is beneficial. In the hub regions, where shape adaption cannot be applied effectively, the deficit in morphing could be compensated by designing rotor blades with a higher tolerance towards incidence. The AFC-induced flow deviation in the second rotor reaches a maximum of 0.5° at approximately 22% of the blade height. With

the typical deformation distribution displayed in Fig. 3, this AFC specific morphing requirement is, however, difficult to satisfy. Additionally, the MFC shape adaption, does not provide sufficient deformation for the test case investigated (NASA rotor 67) and—due to the smaller and, thus, more rigid blades—certainly not for the application in HPC. Possible solutions comprise an adaptation of the way the blade is clamped, to reduce rigidity, or the application to the IGV, which features a lower hub-to-tip ratio. Furthermore, raising the Mach number by raising the mass-flow rate and rotor speed, may increase the effectiveness of the shape adaption.

The deformation results suggest that, while still at a very low technological readiness level, the application of SMA shape adaption allows significantly higher blade deformations. The achievable variations in blade leading-edge metal angle even exceeds the AFC morphing requirement of 2° at the blade tip (Fig. 9), when an AFC stator S1 is combined with the shape-adaptive rotor R2. A deviation from the so far typical span-wise deformation distributions is possible through the application of SMAs. With the camber angle deformation maximum at 35% blade height, the AFC-induced flow deviation distribution could be compensated, provided that the exceeding deformation levels can be adjusted to the AFC requirements. Here, a concurrent design of the injection and shape-adaption system, ideally in a new compressor design with increased rotor chord lengths, may lead to the benefit envisioned. However, the reliable application of SMA actuators in aircraft engines requires further investigations regarding possible effects of fatigue damage due to repeated large deformations.

7 Conclusions and future scope

This research shows how shape adaption and active flow control by means of injection may be used to improve off-design compressor performance. Possible approaches for combining both methods were discussed and current technological limitations, as well as counter-measures, were highlighted.

1. Shape-adaptive rotor blades affect the compressor performance. Especially for elevated inflow Mach numbers, morphing causes a shift in overall mass flow and isentropic efficiencies. The blade deformations attainable, however, are not sufficient to obtain the desired performance improvements.
2. Injection of fluid into the first stator row yields a significant increase in the overall static and total-pressure ratios, as well as a shift towards higher corrected mass-flow rates. Compared to the reference case, the isentropic efficiency decreases slightly towards the surge limit.

3. Stage 2 experiences the strongest AFC-induced performance variations.
4. The injection in stator 1 increases the flow turning and causes a higher incidence towards the subsequent rotor 2. This results in a higher work input in stage 2 and is associated with additional incidence-related losses, especially towards the surge limit.
5. SMA materials allow for sufficiently large blade deformations capable of mitigating the incidence changes induced by the injection of fluid in an upstream stator. However, SMA actuators require further development for their reliable application in aircraft engines. A major issue is the fatigue damage that may occur on the metallic or composite bodies of the blades due to the considerably large deformations.

Future research on this topic should aim at further refining the presented combined approach to realise its maximum potential. This includes the following steps:

- 1). In this study, the same fraction of the inlet mass flow is injected across all operating points. Further performance improvements, as well as a wider operating range, could be obtained by adjusting the AFC mass-flow rates depending on the operating-point.
2. Since the rise in the total-pressure ratio is a result of an increased incidence towards rotor 2, a redesign of the second rotor could lead to even higher aerodynamic loading with reduced incidence-related losses. Shape-variable blades could potentially be used for further enhancing of the operational flexibility of the compressor by means of an operating-point dependent blade deformation.
3. The effect of a shape-adaptive rotor R1 on the overall HPC performance should be investigated, especially in combination with flow injection in the first stator row (S1).
4. SMA material actuators should be developed to become a viable alternative to MFCs.
5. A combined implementation of shape adaption and active flow control likely requires a combined design approach.

Contact address:

Shape adaption

m.seidler@ifas.tu-braunschweig.de

Active flow control

mimic@tfd.uni-hannover.de

Acknowledgements We would like to acknowledge the funding by the Deutsche Forschungsgemeinschaft (DFG, German Research Foundation) under Germany's Excellence Strategy EXC 2163/1 Sustainable and Energy Efficient Aviation Project ID 390881007. We would also like to acknowledge the contribution of the DLR Institute of Propulsion

Technology and MTU Aero Engines AG for providing TRACE. We thank the Leibniz Universität Hannover IT Services (LUIS) for providing computational resources.

Funding Open Access funding enabled and organized by Projekt DEAL.

Declarations

Conflict of interest The authors have no competing interests to declare that are relevant to the content of this article.

Open Access This article is licensed under a Creative Commons Attribution 4.0 International License, which permits use, sharing, adaptation, distribution and reproduction in any medium or format, as long as you give appropriate credit to the original author(s) and the source, provide a link to the Creative Commons licence, and indicate if changes were made. The images or other third party material in this article are included in the article's Creative Commons licence, unless indicated otherwise in a credit line to the material. If material is not included in the article's Creative Commons licence and your intended use is not permitted by statutory regulation or exceeds the permitted use, you will need to obtain permission directly from the copyright holder. To view a copy of this licence, visit <http://creativecommons.org/licenses/by/4.0/>.

References

1. Gunn, E.J., Brandvik, T., Wilson, M.J.: Fan-intake coupling with conventional and short intakes. In: Volume 1: Aircraft Engine; Fans and Blowers; Marine; Wind Energy; Scholar Lecture, p. 06072021. American Society of Mechanical Engineers. <https://doi.org/10.1115/GT2021-58829>
2. Giesecke, D., Friedrichs, J.: Aerodynamic comparison between circumferential and wing-embedded inlet distortion for an ultra-high bypass ratio fan stage. In Volume 2A: Turbomachinery, p. 06172019. American Society of Mechanical Engineers. <https://doi.org/10.1115/GT2019-90425>
3. Bräunling, W.J.G.: Flugzeugtriebwerke: Grundlagen, Aero-Thermodynamik, ideale und reale Kreisprozesse, thermische Turbomaschinen, Komponenten, Emissionen und Systeme. VDI-Buch. Springer Vieweg, Berlin, 4. Aufl. edition (2015). <https://doi.org/10.1007/978-3-642-34539-5>
4. Rick, H.: Gasturbinen und Flugantriebe: Grundlagen, Betriebsverhalten und Simulation. VDI-Buch. Springer Berlin Heidelberg, Berlin (2013). <https://doi.org/10.1007/978-3-540-79446-2>
5. Giesecke, D., Bullert, M., Friedrichs, J., Stark, U.: Optimization of high subsonic, high Reynolds number axial compressor airfoil sections for increased operating range. Proc. GPPS Forum **18**, 1–9 (2018). <https://doi.org/10.5281/ZENODO.1343465>
6. Giesecke, D.: Aerodynamic Design and Performance of an Over-Wing Low Pressure Ratio Fan Stage. Dissertation, Technischen Universität Carolo-Wilhelmina, Braunschweig (2021)
7. Aungier, R.H.: Axial-Flow Compressors: A Strategy for Aerodynamic Design and Analysis. American Society of Mechanical Engineers, New York (2003). <https://doi.org/10.1115/1.801926>
8. Krone, J.H., Huxdorf, O., Riemenschneider, J., Monner, H.P., Schur, F., Friedrichs, J., Wiedemann, M.: Experimental investigation and design of a shape-variable compressor cascade. CEAS Aeronaut. J. **8**(1), 105–127 (2017). <https://doi.org/10.1007/s13272-016-0224-1>
9. Montano, Z., Seidler, M., Riemenschneider, J., Friedrichs, J.: A coupling method for the design of shape-adaptive compressor

- blades. *Appl. Mech.* **3**(1), 182–209 (2022). <https://doi.org/10.3390/applmech3010014>
10. Mazzawy, R.S., Virkler, J.: Variable pitch fan—the solution to achieving high propulsive efficiency turbofan engines. In: SAE Technical Paper Series, SAE Technical Paper Series. SAE International 400 Commonwealth Drive, Warrendale (2009). <https://doi.org/10.4271/2009-01-3103>
 11. Denning, R.M.: Variable pitch ducted fans for stol transport aircraft. In: ASME 1972 International Gas Turbine and Fluids Engineering Conference and Products Show, p. 03261972. American Society of Mechanical Engineers. <https://doi.org/10.1115/72-GT-61>
 12. McAuliffe, B.R., Sjolander, S.A.: Active flow control using steady blowing for a low-pressure turbine cascade. *ASME J. Turbomach.* **41707**, 1223–25 (2004)
 13. Guendogdu, Y., Vorreiter, A., Seume, J.R.: Design of a low solidity flow-controlled stator with coanda surface in a high speed compressor. In: Proc. ASME Turbo Expo, pp. 629–639, Paper No. GT2008-51180 (2008). <https://doi.org/10.1115/GT2008-51180>
 14. Vorreiter, A., Fischer, S., Saathoff, H., Radespiel, R., Seume, J.R.: Numerical investigations of the efficiency of circulation control in a compressor stator. *ASME J. Turbomach.* **134**(2) (2012)
 15. Du, J., Li, Y., Li, Z., Li, J., Wang, Z., Zhang, H.: Improving aerodynamic performance of a highly loaded compressor based on Coanda jet flap. In: Proc. ASME Turbo Expo, Paper No. GT2019-91552 (2019). <https://doi.org/10.1115/GT2019-91552>
 16. Kerrebrock, J.L., Drela, M., Merchant, A.A., Schuler, B.J.: A family of designs for aspirated compressors. In: Proc. ASME Turbo Expo, 98-GT-196 (1997)
 17. Liesner, K., Meyer, R., Lemke, M., Gmelin, C., Thiele, F.: On the efficiency of secondary flow suction in a compressor cascade. In: Proc. ASME Turbo Expo, Paper No. GT2010-22336 (2010). <https://doi.org/10.1115/GT2010-22336>
 18. Siemann, J., Seume, J.R.: Design of an aspirated compressor stator by means of DoE. In: Proc. ASME Turbo Expo, Paper No. GT2015-42474 (2015). <https://doi.org/10.1115/GT2015-42474>
 19. Siemann, J., Krenz, I., Seume, J.R.: Experimental investigation of aspiration in a multi-stage high-speed axial-compressor. In: Proc. ASME Turbo Expo, Paper No. GT2016-56440 (2016). <https://doi.org/10.1115/GT2016-56440>
 20. Geiser, G., Wellner, J., Kügeler, E., Weber, A., Moors, A.: On the simulation and spectral analysis of unsteady turbulence and transition effects in a multistage low pressure turbine. *J. Turbomach.* **141**(5), 01 (2019). <https://doi.org/10.1115/1.4041820>
 21. Smart Material.: MFC Engineering Properties. <https://www.smart-material.com/MFC-product-propertiesV2.html>. Accessed 10 Feb 2024
 22. Hathaway, M.D.: Unsteady flows in a single-stage transonic axial-flow fan stator row. Retrospective theses and dissertations, Iowa State University, Ames (1986)
 23. Seidler, M., Sivamoorthy, K., Friedrichs, J.: Introduction of a streamline curvature design methodology for the vortex design of shape adaptive compressor blading. In: Proceedings of the 14th European Conference on Turbomachinery Fluid Dynamics and Thermodynamics (2021) (**in press**)
 24. Seidler, M., Montano, Z., Friedrichs, J., Riemenschneider, J.: Introduction and evaluation of an aerostructural coupling approach for the design of shape adaptive compressor blading (**in press**)
 25. Roache, P.J.: Perspective: a method for uniform reporting of grid refinement studies. *J. Fluids Eng.* **116**(3), 405–413 (1994). <https://doi.org/10.1115/1.2910291>
 26. Cumpsty, N.A.: Compressor aerodynamics. Krieger Publishing Company, Malabar, Florida, reprint edition 2004 w/new preface, introduction and updated bibliography edition (2004)
 27. Menter, F., Kuntz, M., Langtry, R.B.: Ten years of industrial experience with the SST turbulence model. *Turbul. Heat Mass Transf.* **4**, 625–632 (2003). 10.1.1.460.2814
 28. Menter, F., Langtry, R.B., Likki, S.R., Suzen, Y., Huang, P., Völker, S.: A correlation-based transition model using local variables—part I: model formulation. *ASME J. Turbomach* **128**(3), 413–422 (2006). <https://doi.org/10.1115/1.2184352>
 29. Kato, M., Launder, B.E.: The modelling of turbulent flow around stationary and vibrating square cylinders. In: 9th Symposium on Turbulent Shear Flows, pp. 10.4.1–10.4.6 (1993)
 30. Mimic, D., Sauer, P., Seume, J.R.: Sensitivity of compressor performance and tip-leakage vortices to inhomogeneous casing heat-flux distributions. In: Proceedings of the Global Power and Propulsion Society Xi'an Conference, Paper No. GPPS-TC-2021-0337 (2021). <https://doi.org/10.33737/gpps21-tc-337>
 31. Montano Rejas, Z., Seidler, M., Riemenschneider, J., Friedrichs, J.: Aerodynamic validation for compressor blades' structural morphing concepts. *CEAS Aeronaut. J.* **14**, 139–154 (2023). <https://doi.org/10.1007/s13272-022-00624-z>
 32. Meinicke, N.: Konstruktion und Berechnung der Integration von Flächenaktuatoren in neue Anschlusskonzepte für morphende Triebwerksschaufeln. Master's thesis, German Aerospace Center and Technische Universität Braunschweig (2022)

Publisher's Note Springer Nature remains neutral with regard to jurisdictional claims in published maps and institutional affiliations.